# Computational fluid dynamics modeling of polymer electrolyte membrane fuel cells

Galip H. Guvelioglu, Harvey G. Stenger *

*Chemical Engineering Department, Lehigh University, Bethlehem, PA 18015, USA*

## Abstract

A detailed steady-state isothermal two-dimensional model of a proton exchange membrane fuel cell has been developed. A finite element method was used to solve this multi-component transport model coupled with flow in porous medium, charge balance, electrochemical kinetics, and a rigorous water balance in the membrane. The model-predicted fuel cell performance curves are compared with published experimental results and a good agreement was found. The complex water balance in the membrane was investigated and the operating conditions where the membrane becomes dehydrated were identified. The effects of channel width and bipolar plate shoulder dimensions, porosity, and the relative humidity of the inlet streams on the fuel cell performance are evaluated. It was found that smaller width channels and bipolar plate shoulders were required for high current density operations. As the electrode area under the bipolar plate shoulder increases, the fuel cell benefits more from higher porosity electrodes. The anode gas stream's relative humidity was found to be more critical for fuel cell performance than the cathode gas relative humidity.
© 2005 Elsevier B.V. All rights reserved.

*Keywords:* PEM fuel cells; Fuel cell modeling; Water management; CFD; FEMLAB

## 1. Introduction

Since the early 1990s there has been growing interest in modeling proton exchange membrane (PEM) fuel cells. Earlier models by Bernardi and Vebrunge [1] and Springer et al. [2] are fundamental studies toward understanding PEM fuel cells. The two groups both developed a one-dimensional, isothermal model of a membrane electrode assembly (MEA). Bernardi and Vebrunge [1] studied the net water flux through the membrane and Springer et al. [2] included variable membrane hydration in his model. Fuller and Newman [3] developed a two-dimensional (2D) model to study water and thermal management issues and used concentrated solutions theory for transport in the membrane. Nguyen and White [4] studied the effects of various forms of gas humidification on cell performance, heat and water management and reported that back diffusion of water from

the cathode to anode is insufficient to keep the membrane hydrated at high current density operations. They consequently concluded that the fuel and oxidant must both be humidified.

Variable degrees of water flooding in the catalyst layers and electrode backing regions was studied by Baschuk and Li [5] in a one-dimensional model. Later Baschuk and Li [6] also examined the issue of carbon monoxide poisoning in PEM fuel cells.

In recent years, a general trend of using computational fluid dynamics (CFD) to model PEM fuel cells has evolved. Gurau et al. [7] developed the first real two-dimensional model of a fuel cell with flow channels and MEA. This "along-the-channel" model studied the effects of composition change of the reactants inside the channels. Um et al. [8] developed a two-dimensional transient, "along-the-channel" model and studied the change of current density with changing cell potential. Um and Wang [9] extended the work to the third dimension and also studied the effects of flow channel geometry and layout. A group at the Electrochemical Re-

* Corresponding author. Tel.: +1 610 758 4791; fax: +1 610 758 5057.
  *E-mail address:* hgs0@lehigh.edu (H.G. Stenger).

**Nomenclature**

| | |
|---|---|
| $a$ | water activity |
| $c$ | concentration (mol m$^{-3}$) |
| $c_w$ | mass concentration of water in the membrane (kg m$^{-3}$) |
| $D_{ij}$ | binary diffusivity (m$^2$ s$^{-1}$) |
| $D_w$ | water diffusivity in the membrane (m$^2$ s$^{-1}$) |
| $EW_m$ | equivalent molecular weight |
| $F$ | Faraday's constant (96487 C (mol)$^{-1}$) |
| $\boldsymbol{I}$ | local current density vector (A m$^{-2}$) |
| $i_0$ | exchange current density |
| $k$ | constant reaction parameter |
| $k_p$ | permeability (m$^2$) |
| $L$ | length (m) |
| $n_d$ | drag coefficient |
| $M$ | molecular weight (kg mol$^{-1}$) |
| $\boldsymbol{N}$ | molar flux vector (mol m$^{-2}$ s$^{-1}$) |
| $\boldsymbol{N_w}$ | net water mass flux vector (kg m$^{-2}$ s$^{-1}$) |
| $p$ | pressure (Pa) |
| $R$ | universal gas constant (8.314 J mol$^{-1}$ K$^{-1}$) |
| $T$ | temperature (K) |
| $\boldsymbol{u}$ | velocity vector (m s$^{-1}$) |
| $V_{oc}$ | open cell potential (V) |
| $w$ | weight fraction |
| $x$ | mole fraction |

*Greek letters*

| | |
|---|---|
| $\alpha$ | transfer coefficient |
| $\sigma$ | conductivity (S m$^{-1}$) |
| $\varepsilon$ | porosity |
| $\gamma$ | reaction order |
| $\lambda$ | membrane water content (mol H$_2$O (mol SO$_3{}^-$)$^{-1}$) |
| $\mu$ | viscosity (kg m$^{-1}$ s$^{-1}$) |
| $\eta$ | overpotential (V) |
| $\rho$ | density (kg m$^{-3}$) |

*Subscripts*

| | |
|---|---|
| avg | average value |
| $i, j$ | components, H$_2$, and H$_2$O for the anode, O$_2$, H$_2$O, and N$_2$ for the cathode |
| s | gas distribution electrode |
| m | membrane |
| w | water in the membrane |

*Superscripts*

| | |
|---|---|
| eff | effective |
| ref | reference conditions |

search Center of Pennsylvania State University developed a large-scale CFD model [10] and studied the two-phase transport issues in PEM fuel cells [11]. Berning et al. [12] developed a three-dimensional model, conducted parametric studies on operating pressure and temperature as well as geomet-

rical and material properties [13], and developed a two-phase model [14].

All of the CFD work done by the previously cited authors was aimed toward understanding the PEM fuel cell and simulating the performance of a given design. However, those models were not suitable for optimization of the fuel cell design and other units that comprise the fuel cell system. To our knowledge optimization of PEM fuel cell design using CFD has been attempted only by Grujicic and Chittajallu [15]. However, the model used by Grujicic and Chittajallu [15] assumes constant membrane hydration meaning that membrane conductivity changes and the complex water balance was not investigated.

Currently, there are several commercial CFD packages from various vendors that can be used for modeling PEM fuel cells [16–19]. The nature of modeling PEM fuel cells requires uncommon water balance equations, which these commercial CFD packages can add and solve. CFD modeling is computationally demanding especially for three-dimensional models. Because the geometric dimensions of the various fuel cell regions range several orders of magnitude, the models require very small elements to capture the details with accurate resolution. For example, the typical anode and cathode catalyst layer thickness of PEM fuel cells are on the order of 10–20 μm, however, the height and width are 10–20 cm requiring at least a million elements for even a small 7 cm by 1 cm section of a fuel cell [10]. The computational cost of CFD modeling an entire cell is large and we are not yet able to simulate an entire fuel cell stack. However, the interactions between cells in a stack are critical for water and thermal management since the cells located at the middle section of the stack will require extra means of cooling.

Considering the computational cost of CFD modeling of PEM fuel cells, using a three-dimensional fuel cell stack model is not practical in most computing environments. The purpose of this study is to develop a fast, robust, and detailed two-dimensional CFD model that can predict effects of channel geometry, and water management, and that can be used for optimization of the fuel cell components, design, and operating conditions for different applications.

## 2. Problem description

A schematic illustration of a PEM fuel cell divided into seven sub-regions is shown in Fig. 1. The membrane electrode assembly consists of an ion exchange membrane with a thickness of 100–250 μm sandwiched between two Pt based catalyst layers with a thickness of 10–20 μm and backed by porous gas distribution electrodes (GDE), which is usually carbon cloth with a thickness of 200–300 μm. The MEA is then sandwiched between two bipolar plates. These plates serve as a manifold for the transfer of feed and products in and out of the fuel cell and as the current collector.
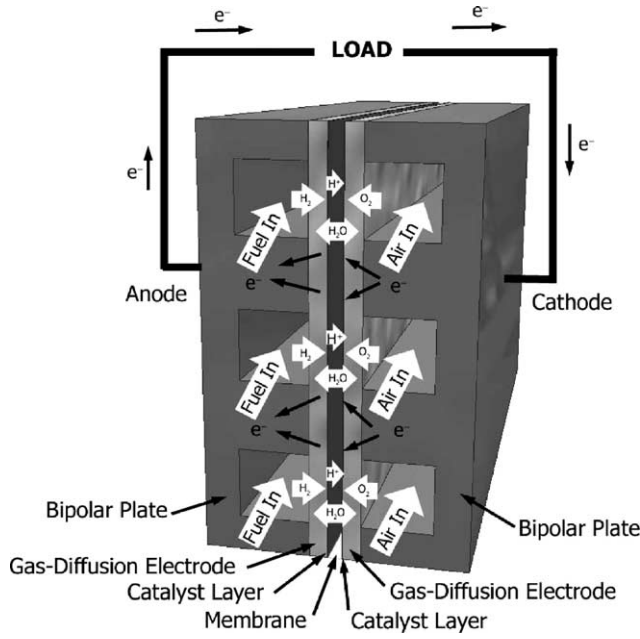
Fig. 1. Schematic illustration of the PEM fuel cell.

The heart of a fuel cell is the active catalyst layers, since at these regions the four ingredients: membrane, catalyst, electronic conductor, and chemical reactants, required for the fuel cell electrochemistry, exist together.

Hydrogen, which is usually humidified, enters the anode gas chamber, transports through the porous electrode by convection and diffusion, and dissolves into the membrane phase of the anode catalyst layer. The hydrogen is subsequently oxidized, the membrane is replenished with protons, and the carbon conductor receives electrons by the anode reaction:

$$2H_2 \rightarrow 4H^+ + 4e^- \tag{R-1}$$

The oxidant, $O_2$ in air, which is usually humidified, enters the cathode gas chamber, transports through the porous electrode by convection and diffusion and dissolves into the membrane phase of the active catalyst layer. Protons in the membrane pores, coming from the anode side, react with dissolved $O_2$ at catalyst sites in the active layer to produce water in the electrochemical reaction:

$$O_2 + 4H^+ + 4e^- \rightarrow 2H_2O \tag{R-2}$$

A comprehensive review of PEM fuel cell design and manufacturing is done by Mehta and Cooper [20].

The design of PEM fuel cells requires a strong understanding of the processes such as mass, momentum and energy
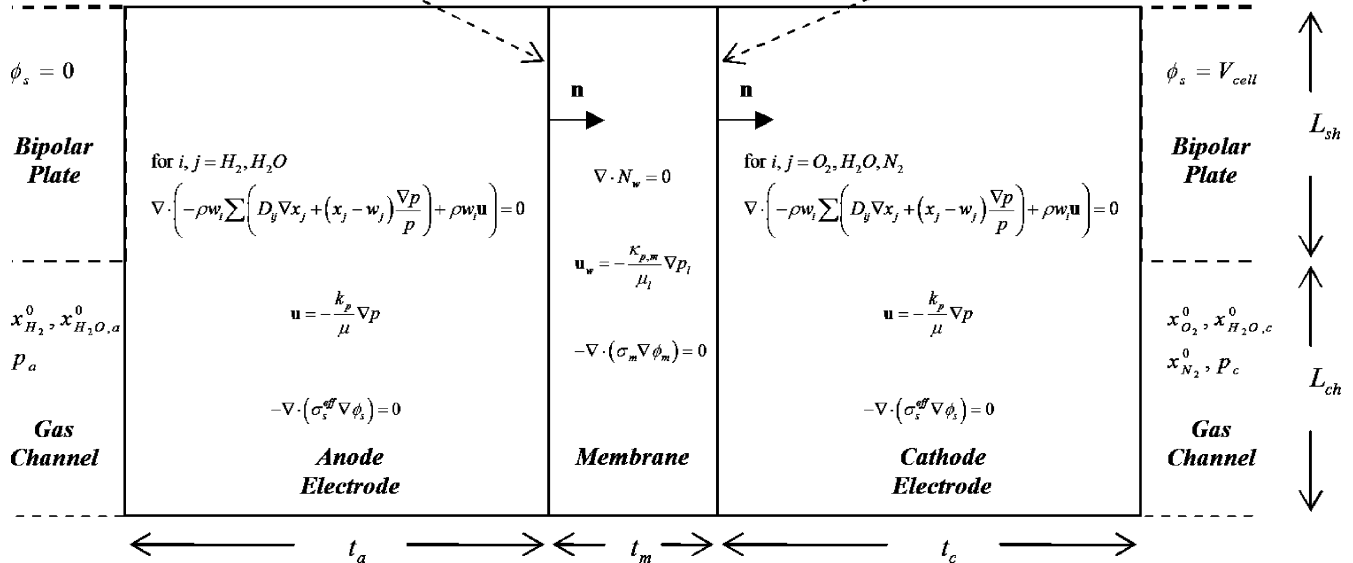


Fig. 2. Computational domain and governing equations.

transport, electrochemical reactions, and charge balance taking place inside the fuel cell. A PEM fuel cell's performance is significantly affected by the water content of the membrane due to the nature of the membrane material. Greater membrane hydration means higher conductivity, less potential loss at the membrane thus higher cell voltage and power. Water balance in the fuel cell is a complex phenomenon and needs to be controlled accurately for the successful design and operation of fuel cells.

A typical cell thickness is in the range of 1–2 mm, this includes the seven sub-regions as well as the bipolar plates. The length and width of a typical single cell is between 10 and 20 cm. This order of magnitude difference in dimensions requires simplification of the fuel cell to 2D geometry in order to minimize the number of mesh elements. The thickness of the active catalyst layers is about 10 μm, which is very small with respect to other cell components, and can be treated as reactive boundaries. The selected 2D domain includes the gas distribution electrodes, catalyst layers as reactive boundaries and membrane and shown in Fig. 2.

Model assumptions:

- steady-state operation,
- isothermal operation,
- ideal gas mixtures,
- single-phase model,
- isotropic and homogeneous electrodes and membrane,
- the membrane is considered impermeable for the gas phase which was supported by the findings of an earlier study [1],
- negligible contact resistance,
- minimal membrane swelling.

Model simplifications:

- two-dimensional model,
- catalyst layers as reactive boundaries.

The PEM fuel cell model developed is a comprehensive two-dimensional, isothermal, steady-state model providing a detailed description of the following transport phenomena:

- multi-component flow,
- diffusion of reactants through the porous electrodes,
- electrochemical reactions,
- transport of electrons through the electrodes,
- water balance in the membrane.

The equations governing these processes include:

- ionic balance in electrodes and membrane,
- the Maxwell–Stefan equations for multi-component diffusion and convection in gas distribution channels and gas distribution layers,
- Darcy's law for the flow of species in porous electrodes,
- water balance and water flux in the membrane governed by diffusion, convection, and electro-osmotic drag.

## 3. Model equations

### 3.1. Gas distribution electrodes

In the gas distribution electrodes, Darcy's law is used to model the flow in this porous media with the pressure gradient as the driving force. In a porous structure, the global transport of momentum by shear stresses in the fluid is negligible because the pore walls impede transport of this momentum to the fluid outside the individual pores. Since a detailed description at the resolution of a pore is not practical in most models, homogenization of the porous and fluid media is a common approach. Darcy's law is based upon homogenization of the porous and fluid media into one single medium and does not require a detailed geometrical description of the pore structure.

Darcy's law states that the velocity vector is determined by the pressure gradient, the fluid viscosity, and the structure of the porous media represented with the following equation:

$$\boldsymbol{u} = -\frac{k_{\mathrm{p}}}{\mu}\nabla p \tag{1}$$

where $\boldsymbol{u}$ is the velocity vector, $k_{\mathrm{p}}$ the permeability, $\mu$ the gas viscosity, and $p$ is the pressure. Variables, descriptions, and their units are given in Nomenclature section of this paper.

For multi-component diffusion in gases at low density it has been shown that Maxwell–Stefan is a good approximation [21].

$$\nabla x_i = -\sum_{j=1}^{N} \frac{1}{cD_{ij}}(x_j \boldsymbol{N}_i - x_i \boldsymbol{N}_j), \quad i = 1, 2, \ldots, N \tag{2}$$

where $D_{ij}$ is the binary diffusivity of $i$ and $j$, $c$ the concentration, $x_i$ the mole fraction of component $i$, and $\boldsymbol{N}_i$ is the molar flux vector of component $i$. Experimentally obtained binary diffusivities, $D_{ij}^0$ at atmospheric pressure $p_{\mathrm{atm}}$ and reference temperature $T_0$ shown in Table 1 are scaled to operating temperature and pressure according to [21]:

$$D_{ij} = D_{ij}^0(T_0, p_0)\frac{p_0}{p}\left(\frac{T}{T_0}\right)^{1.5} \tag{3}$$

The species balances in the porous gas diffusion electrodes are solved with the following equation:

$$\nabla \cdot \left(-\rho w_i \sum \left(D_{ij}\nabla x_j + (x_j - w_j)\frac{\nabla p}{p}\right) + \rho w_i \boldsymbol{u}\right) = 0 \tag{4}$$

Table 1
Binary diffusivities and reference temperatures at 1 atm [13]

| Gas pair | Reference temperature, $T_0$ [K] | Binary diffusivity, $D_{ij}(T_0, p_0)$ [m$^2$ s$^{-1}$] |
|---|---|---|
| $D_{\mathrm{H_2-H_2O}}^0$ | 307.1 | $9.15 \times 10^{-5}$ |
| $D_{\mathrm{O_2-H_2O}}^0$ | 308.1 | $2.82 \times 10^{-5}$ |
| $D_{\mathrm{O_2-N_2}}^0$ | 293.2 | $2.2 \times 10^{-5}$ |
| $D_{\mathrm{H_2O-N_2}}^0$ | 307.5 | $2.56 \times 10^{-5}$ |

where $i = H_2$ and $H_2O$ for the anode and $i = O_2$, $H_2O$, and $N_2$ for the cathode side, $w$ the weight fraction, and $\rho$ is the gas mixture density calculated with:

$$\rho = \frac{\sum_i x_i \cdot MW_i}{RT} p \tag{5}$$

However, due to the porous structure of the electrodes the binary diffusivities need to be corrected for the porosity $\varepsilon$ of the electrode media. This is done with the Bruggeman correlation [1]:

$$D_{ij}^{\text{eff}} = D_{ij} \varepsilon^{1.5} \tag{6}$$

where $D_{ij}$ are the binary diffusivities from Table 1, corrected for the operating temperature and pressure with Eq. (3).

The Maxwell–Stefan and Darcy's equations are coupled through the velocity vector $\boldsymbol{u}$, and density $\rho$. In addition to mass and momentum balances in the porous electrodes the charge balance is also solved in the electrodes with the continuity relationship:

$$-\nabla \cdot (\sigma_s^{\text{eff}} \nabla \phi_s) = 0 \tag{7}$$

where $\sigma_s^{\text{eff}}$ is the effective conductivity and $\phi_s$ is the potential in the electrode.

## 3.2. Membrane

The permeability of the membrane to hydrogen, oxygen, and nitrogen is low and can be neglected [1]. Thus, only water and protons are transported and each obeys the principle of mass conservation, with the charge balance in the membrane accounted for with the continuity relationship:

$$-\nabla \cdot (\sigma_m \nabla \phi_m) = 0 \tag{8}$$

where $\phi_m$ is the membrane potential and $\sigma_m$ is the membrane conductivity which is a function of membrane water content $\lambda$, i.e., the local $[H_2O]/[SO_3^-]$ ratio in the membrane. Springer et al. [2] presented the following empirical expression for the conductivity of Nafion® membrane based on their experiments:

$$\sigma_{30} = 0.5139\lambda - 0.326, \quad \text{for } \lambda > 1 \tag{9}$$

where $\sigma_{30}$ is the membrane conductivity $[S\,m^{-1}]$ measured at 30 °C and then corrected to operating temperature $T$ with:

$$\sigma_m = \exp\left[1268\left(\frac{1}{303} - \frac{1}{T}\right)\right] \sigma_{30} \tag{10}$$

At steady-state, the water balance in the membrane reduces to:

$$\nabla \cdot \boldsymbol{N}_w = 0 \tag{11}$$

where $\boldsymbol{N}_w$ is the net water mass flux vector. Positive values for $\boldsymbol{N}_w$ mean net water flux from anode to cathode and negative values are from cathode to anode.

The mass flux of water in the membrane is governed by three processes: electro-osmotic drag due to the flow of protons, diffusion due to a concentration gradient, and convection due to pressure gradient. These three processes lead to:

$$\boldsymbol{N}_w = \frac{n_d \cdot \boldsymbol{I} \cdot M_{H_2O}}{F} - D_w \nabla c_w - c_w \boldsymbol{u}_w \tag{12}$$

where $c_w$ is the mass concentration of water, $D_w$ the diffusion coefficient of water in the membrane, $n_d$ the electro-osmotic drag coefficient, $\boldsymbol{I}$ the local current density vector, $M_{H_2O}$ the molecular weight of water, and $F$ is the Faraday's constant. The velocity of the water in the membrane, $\boldsymbol{u}_w$ follows Darcy's law Eq. (1).

The membrane water diffusivity is related to the temperature and water content of the membrane with the following relationship of Motupally et al. [22].

$$D_w = \begin{cases} 3.1 \times 10^{-7}\lambda[\exp(0.28\lambda) - 1]\exp(-2346/T), & \lambda \leq 3 \\ 4.17 \times 10^{-8}\lambda[1 + 161\exp(-\lambda)]\exp(-2346/T), & \lambda > 3 \end{cases} \tag{13}$$

The drag coefficient of water in the membrane, $n_d$ also depends on the membrane water content. According to Zawodzinkski et al. [23], the drag coefficient is equal to unity in the range of water content from $\lambda = 5$ to 14. Because the drag coefficient must drop to zero at $\lambda = 0$, below a water content of 5, a linear relation between the drag coefficient and water content is used. The drag coefficient for the membrane in equilibrium with liquid water increases from $n_d = 1$ to 2.5 as the water content, $\lambda$ increases from 14 to 22 reported by the previous study of Zawodzinkski et al. [24].

$$n_d = \begin{cases} 0.2\lambda, & \text{for } \lambda < 5 \\ 1, & \text{for } 5 \leq \lambda \leq 14 \\ 0.1875\lambda - 1.625, & \text{for } \lambda > 14 \end{cases} \tag{14}$$

After the water concentration is calculated in the membrane with Eqs. (11) and (12), the water content of the membrane is calculated with [4]:

$$\lambda = \frac{EW_m \cdot c_w}{\rho_m \cdot M_{H_2O}} \tag{15}$$

where $\rho_m$ is the dry membrane density and $EW_m$ is the equivalent molecular weight of the membrane.

## 3.3. Boundary conditions

The governing equations, boundary conditions and normal vectors at the inside boundaries are summarized in Fig. 2, the other remaining boundaries are either insulation or symmetry. Due to symmetry only the half of the gas channels and bipolar plate shoulders are modeled.

### 3.3.1. Catalyst reactive boundaries

Water can enter the membrane only from the anode and cathode boundaries. The pressures at these boundaries are set

to the solved for anode and cathode pressures. However, the boundary condition for the water concentration offers a challenge due to the hydrophobic nature of the membrane. Over the entire range of normal operating conditions, the activity coefficient of water in the membrane is greater than unity if one assumes a Raoult's law relationship between water activity and membrane water content. In theory one expects that the membrane in contact with saturated vapor and liquid water to have the same amount of water content, however experiments conducted on several polymer polymer/solvent systems reports different water uptake from liquid water versus saturated water vapor. The phenomena was first reported in 1903 by Schroeder and thus called Schroeder's paradox.

The hydrophobic nature of the membrane and Schroeder's paradox are treated with equivalent boundary conditions. In this approach, a fit of the experimental relationship of the water content of the membrane to the water vapor activity, $a$ reported by Springer et al. [2] is used to calculate the water content at the membrane boundaries using:

$$\lambda = 0.043 + 17.81a - 39.85a^2 + 36a^3, \quad \text{for } 0 < a \le 1 \tag{16}$$

which is used with Eq. (15) to calculate the concentration of water at the anode and cathode gas channel boundaries.

As the water mole fraction exceeds saturation, a linear relation is assumed between the water content and water activity (Springer et al. [2]):

$$\lambda = 14 + 1.4(a - 1), \quad \text{for } 1 < a \le 3 \tag{17}$$

The activity in the vapor phase is:

$$a = \frac{x_{H_2O}p}{p_{sat}} \tag{18}$$

where $p_{sat}$ is the saturation pressure of water calculated with [25]:

$$p_{sat} = \exp\left(73.648 - \frac{7258.2}{T} - 7.3037 \log T + 4.1653 \times 10^{-6}T^2\right) \tag{19}$$

Because the catalyst layers are very thin compared to other elements of the fuel cell, they are treated as reactive boundaries. The Butler–Volmer kinetic equation is used to obtain the local current density distribution at the catalyst surface [26].

$$i_a = i_{0,a}\left[\exp\left(\alpha_a^- \frac{F}{RT}\eta\right) - \exp\left(-\alpha_c^- \frac{F}{RT}\eta\right)\right] \tag{20}$$

$$i_c = i_{0,c}\left[\exp\left(\alpha_a^+ \frac{F}{RT}\eta\right) - \exp\left(-\alpha_c^+ \frac{F}{RT}\eta\right)\right] \tag{21}$$

where $i_{0,a}$ and $i_{0,c}$ are the exchange current densities of the anode and cathode, respectively, $\eta$ the activation overpotential, and $\alpha$ is the transfer coefficient. The exchange current densities are scaled from the reference exchange current densities

Table 2
Butler–Volmer kinetic parameters

| Symbol | Value | Reference |
|---|---|---|
| $\alpha_a^-$, anode; anodic transfer coefficient | 0.5 | [13] |
| $\alpha_c^-$, anode; cathodic transfer coefficient | 0.5 | [13] |
| $\alpha_a^+$, cathode; anodic transfer coefficient | 1 | [13] |
| $\alpha_c^+$, cathode; cathodic transfer coefficient | 1 | [13] |
| $k_a$, anode rate constant ((A m$^{-2}$) (m$^3$ mol$^{-1}$)$^{0.5}$) | 533 | Estimated |
| $k_c$, cathode rate constant ((A m$^{-2}$) (m$^3$ mol$^{-1}$)) | 0.018 | Estimated |
| $\gamma_{O_2}$, concentration parameter | 1 | [8] |
| $\gamma_{H_2}$, concentration parameter | 0.5 | [8] |

with the following expressions [1]:

$$i_{0,a} = i_{0,a}^{ref}\left(\frac{c_{H_2}}{c_{H_2}^{ref}}\right)^{\gamma_{H_2}}\left(\frac{c_{H^+}}{c_{H^+}^{ref}}\right)^{\gamma_{H^+,a}} \tag{22}$$

$$i_{0,c} = i_{0,c}^{ref}\left(\frac{c_{O_2}}{c_{O_2}^{ref}}\right)^{\gamma_{O_2}}\left(\frac{c_{H^+}}{c_{H^+}^{ref}}\right)^{\gamma_{H^+,c}} \tag{23}$$

where $i_{0,a}^{ref}$ and $i_{0,c}^{ref}$ are the reference exchange current densities for anode and cathode reactions at reference conditions, and $\gamma$ is the reaction orders with respect to hydrogen, proton, and oxygen for the anode and cathode reactions. Assuming concentration of protons at the anode and cathode is constant, Eqs. (22) and (23) can then be simplified:

$$i_{0,a} = k_a \cdot c_{H_2}{}^{\gamma_{H_2}} \tag{24}$$

$$i_{0,c} = k_c \cdot c_{O_2}{}^{\gamma_{O_2}} \tag{25}$$

where $k_a$ and $k_c$ are constants that dependent on the catalyst layer properties. Table 2 lists the known parameter values of Eqs. (20)–(25).

For the cathode reaction, the activation overpotential is defined as:

$$\eta = \phi_s - \phi_m - V_{oc} \tag{26}$$

where $V_{oc}$ is the thermodynamic open circuit potential for the overall reaction:

$$O_2 + 2H_2 \rightarrow 2H_2O \tag{R-3}$$

and is calculated using the Nernst law [26],

$$V_{oc} = 1.229 - 0.9 \times 10^{-3}(T - 298) + 2.3\frac{RT}{4F}\log(p_{H_2}^2 p_{O_2}) \tag{27}$$

This reduces to [27]:

$$V_{oc} = 0.2329 + 0.0025 \times T \tag{28}$$

For the anode reaction, the activation overpotential is the difference between the electrode and the membrane potentials and the open circuit potential of the anode is based on the standard hydrogen electrode:

$$\eta = \phi_s - \phi_m \tag{29}$$

The concentrations at the reactive boundary are calculated from the mole fractions of species obtained by the transport relations shown in Fig. 2.

For the catalyst layer between the anode GDE and the membrane, the current fluxes are given with Eqs. (30) and (31):

$$\boldsymbol{n} \cdot (-\sigma_s \nabla \phi_s) = -i_a \tag{30}$$

$$\boldsymbol{n} \cdot (-\sigma_m \nabla \phi_m) = i_a \tag{31}$$

The permeability of the membrane for all components except water is assumed to be zero and the consumption of reactants and formation of products at the catalyst reactive boundary are obtained by coupling the hydrogen flux to the local current density at the boundary.

$$\boldsymbol{n} \cdot \left( -\rho w_{H_2} \sum_{j=H_2,H_2O} \left( D_{H_2 j} \nabla x_j \right. \right.$$
$$\left. \left. +(x_j - w_j)\frac{\nabla p}{p} \right) + \rho w_{H_2} \boldsymbol{u} \right) = -\frac{i_a}{2F} M_{H_2} \tag{32}$$

The mass flux of water at the anode GDE–catalyst–membrane boundary is equal to the membrane water flux at the boundary and overall mass balance of water at anode is obtained by coupling through the momentum balance with the following equation:

$$\boldsymbol{n} \cdot \boldsymbol{u} = \frac{\left( -\frac{i_a}{2F} M_{H_2} - N_w \right)}{\rho} \tag{33}$$

The current flux at the cathode boundary between electrode and membrane are given with Eqs. (34) and (35), respectively.

$$\boldsymbol{n} \cdot (-\sigma_s \nabla \phi_s) = i_c \tag{34}$$

$$\boldsymbol{n} \cdot (-\sigma_m \nabla \phi_m) = -i_c \tag{35}$$

The mass flux of oxygen at the cathode catalyst boundary is obtained by:

$$\boldsymbol{n} \cdot \left( -\rho w_{O_2} \sum_{j=O_2,H_2O,N_2} \left( D_{O_2 j} \nabla x_j \right. \right.$$
$$\left. \left. +(x_j - w_j)\frac{\nabla p}{p} \right) + \rho w_{O_2} \boldsymbol{u} \right) = \frac{i_c}{4F} M_O \tag{36}$$

For water:

$$\boldsymbol{n} \cdot \left( -\rho w_{H_2O} \sum_{j=O_2,H_2O,N_2} \left( D_{H_2O j} \nabla x_j \right. \right.$$
$$\left. \left. +(x_j - w_j)\frac{\nabla p}{p} \right) + \rho w_{H_2O} \boldsymbol{u} \right) = -\frac{i_c}{2F} M_{H_2O} + N_w \tag{37}$$

Table 3
Physical property parameters

| Symbol | Value | Reference |
|---|---|---|
| $k$, permeability of the GDE (m$^2$) | $1.76 \times 10^{-11}$ | [3] |
| $\mu_a$, viscosity of anode gas (Pa s) | $1.378 \times 10^{-5}(T/298)^{1.02}$ | [32] |
| $\mu_c$, viscosity of anode gas (Pa s) | $1.094 \times 10^{-5}(T/298)^{1.05}$ | [32] |
| $\mu_i$, viscosity of water in the membrane (Pa s) | $3.56 \times 10^{-4}$ | [1] |
| $\sigma_s^{eff}$, conductivity of the GDE (S m$^{-1}$) | 570 | [31] |
| $k_p$, hydraulic permeability of membrane (m$^2$) | $1.8 \times 10^{-18}$ | [3] |
| $\rho_m^{dry}$, dry membrane density (kg m$^{-3}$) | 1980 | [10] |
| EW$_m$, equivalent molecular weight (kg mol$^{-1}$) | 1.1 | [10] |

And the momentum flux at the boundary is given by:

$$\boldsymbol{n} \cdot \boldsymbol{u} = \frac{\left( \frac{i_c}{4F} M_{O_2} - \frac{2i_c}{4F} M_{H_2O} + N_w \right)}{\rho} \tag{38}$$

The conservation of nitrogen in the cathode is obtained by solving Eqs. (36)–(38) together, yielding zero net nitrogen flux at the GDE–catalyst–membrane boundary.

### 3.3.2. Bipolar plate shoulder–GDE boundaries

The mass and momentum transport boundary conditions between the bipolar plate shoulders and the gas distribution electrodes are all insulation. The boundary condition for the charge balance in the electrodes is set to zero potential at the anode and set equal to the operating cell potential $V_{cell}$ at the cathode.

### 3.3.3. Channel–GDE boundaries

The fuel and oxidant streams enter and leave the GDEs through the boundary between the channels and GDEs. The pressure of the fuel and oxidant streams are set at these boundaries to the anode and cathode operating pressures times the mole fraction of components. Pure hydrogen is used as a fuel and air is used for the oxidant. The fuel and oxidant streams are fully humidified at the cell operating temperature and pressures for both anode and cathode for the base case.

The partial pressures of water at the anode and cathode boundaries are calculated from Eq. (19), and are divided by the operating pressure to obtain the mole fraction of water. The remaining components are hydrogen at the anode, and oxygen and nitrogen with a stoichometric ratio of 0.21/0.79 at the cathode.

The physical property parameters are shown in Table 3.

## 4. Solution technique

A finite element computational fluid dynamics package, FEMLAB® was used to solve the non-linear system of equations [19]. The following physics application modes in

FEMLAB® and FEMLAB® Chemical Engineering Module were used for solving the dependent variables:

- Darcy's law for pressure in the porous GDEs ($p$);
- Maxwell–Stefan multi-component diffusion and convection: for weight fraction of oxygen and water at the cathode gas channels and GDE ($w_{O_2}$ and $w_{H_2O,c}$) and weight fraction of hydrogen at the anode gas channels and GDE ($w_{H_2}$);
- conductive media DC application mode for charge balance in GDE and membranes ($\phi_s$ and $\phi_m$);
- general PDE form is used to solve for hydraulic pressure and water concentration in the membrane ($p_w$ and $c_w$).

The equations and boundary conditions were outlined in Fig. 2.

FEMLAB® uses a triangular mesh for 2D geometries. Extensive numerical tests were performed and it was found that 1800 mesh elements provided satisfactory spatial resolution for the base case geometry (Table 4) and the solution was found to be independent of the grid size with further refinement.

A stationary non-linear solver was used together with Direct (UMFPACK) linear system solver. The relative tolerance for the error criteria was $1 \times 10^{-4}$ and because the dependent variables vary greatly in magnitude, manual scaling of the dependent variables was used to improve numerical convergence. The manual scaling values are kept constant and were selected such that the magnitude of the scaled degrees of freedom was equal to one.

The model was created and tested in FEMLAB® graphical user interface and then saved as a MATLAB® M-File [28]. Performance curves were obtained by varying the operating potential, i.e., $V_{cell}$ within a loop. Sensitivity analysis of cell design and operating conditions on the fuel cell performance was conducted by putting "for loops" in MATLAB® for changing parameters and calling the FEMLAB® non-linear solver with updated parameters. The model geometry was updated and re-meshed only when a geometric dimension was changed thus saving computational time. The 2D simulation for each operating cell potential converged in 30–400 s, the larger being for the high current density and limiting reactant cases. The majority of the runs were completed under 150 s on an Intel Pentium® 4 3.2 GHz CPU with 1 GB of DDRam.

## 5. Results and discussion

### 5.1. Model validation

The anode and cathode reaction constants, $k_a$ and $k_c$ were adjusted to fit the published single cell experimental results of Ticianelli et al. [29]. The average current density at the catalyst layer was calculated with Eq. (39), and compared
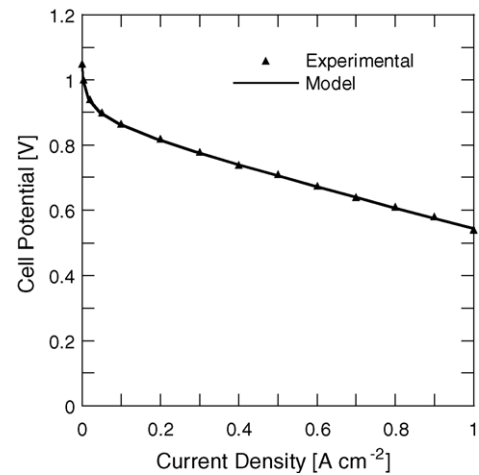


Fig. 3. Comparison of the predicted and measured [29] cell polarization curves.

Table 4
Base case geometric parameters

| Parameter | Value |
|---|---|
| $L_{ch}$, half of the gas channel length due to symmetry (m) | $0.5 \times 10^{-3}$ |
| $L_{sh}$, half of the bipolar shoulder length due to symmetry (m) | $0.5 \times 10^{-3}$ |
| $t_a$ and $t_c$, anode and cathode gas distribution electrode thickness (m) | $2.6 \times 10^{-4}$ |
| $t_m$, membrane thickness (m) | $2.3 \times 10^{-4}$ |
| $\varepsilon$, gas porosity of the anode and cathode GDE | 0.6 |

with experimental results as shown in Fig. 3.

$$I_{avg} = \frac{1}{L_{sh} + L_{ch}} \int_0^{L_{sh}+L_{ch}} I(y)\mathrm{d}y \tag{39}$$

The fuel cell dimensions and operating conditions are tabulated in Tables 4 and 5, respectively. The estimated reference exchange current density for the anode is so large that the activation overpotential is very small compared to the cathode activation overpotential, which is in accordance with experimental findings [29].

Table 5
Operating condition parameters

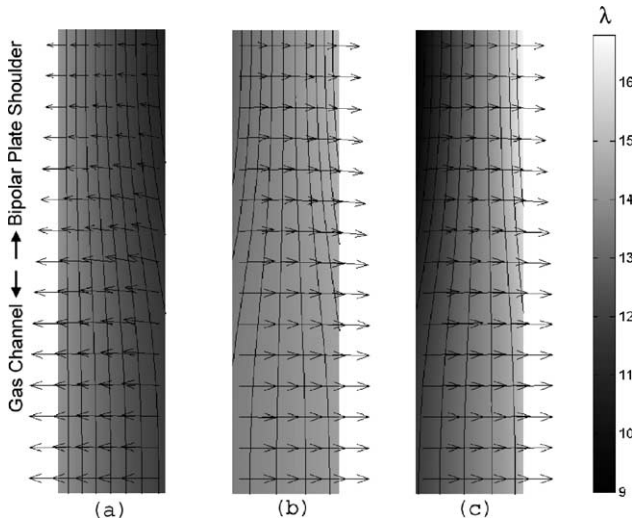| Symbol | Value |
|---|---|
| $T$, temperature (K) | 353 |
| $p_a$, anode side pressure (Pa) | 303975 |
| $p_c$, cathode side pressure (Pa) | 506625 |
| $x_{O_2}^0$, cathode feed oxygen mole fraction | 0.1904 |
| $x_{H_2O,c}^0$, cathode feed water mole fraction | 0.0934 |
| $x_{N_2}^0$, cathode feed nitrogen mole fraction | $1 - x_{O_2}^0 - x_{H_2O,c}^0$ |
| $x_{H_2}^0$, anode feed hydrogen mole fraction | 0.8444 |
| $x_{H_2O,a}^0$, anode feed water mole fraction | $1 - x_{H_2}^0$ |

Fig. 4. Membrane water content ($\lambda$) and net water flux vectors at three different current densities: (a) $V_{cell} = 0.9\,V$, i.e., $I_{avg} = 0.05\,A\,cm^{-2}$, (b) $V_{cell} = 0.7\,V$, i.e., $I_{avg} = 0.52\,A\,cm^{-2}$, and (c) $V_{cell} = 0.5\,V$, i.e., $I_{avg} = 1.13\,A\,cm^{-2}$ (left side is the anode and right side is the cathode).



Fig. 5. Effect of channel geometry on the cell performance.

### 5.2. Water balance

While the published experimental current voltage curves give data on performance of the cell, membrane water content data is limited [30]. The calculated membrane water content and the net water flux are shown in Fig. 4 for three different operating potentials (current densities). At low current densities the water diffusive flux is from anode to cathode as the water content is higher at the anode side in Fig. 4a. At low current densities the migration of water due to proton flow and the diffusive flux is less than the convective flux, thus the net water flux is from cathode to anode shown by the net water flux vectors. As the current density increases the amount of water generated at the cathode side increases and thus the water content of the membrane is higher at the cathode side. Even though the diffusive water flux is from cathode to anode, the migration flux overcomes the diffusive and convective fluxes and the net water flux is from anode to cathode (Fig. 4b). The convective flux of water is from cathode to anode due to the pressure gradient between the two sides and does not change with increasing current density. The effect of the bipolar shoulders on the water content of the membrane can clearly be seen in Fig. 4b contours. The water content gradient is higher at the upper section of the model geometry where the bipolar plates touch the electrodes. As the cell is operated at higher current densities the migrative flux exceeds the diffusive and convective fluxes significantly and dehydration of the membrane at the anode side where the bipolar plate touches the electrodes can be seen in Fig. 4c.

The average water content of the membrane was calculated by integrating the water content in the membrane and dividing it by the total membrane area:
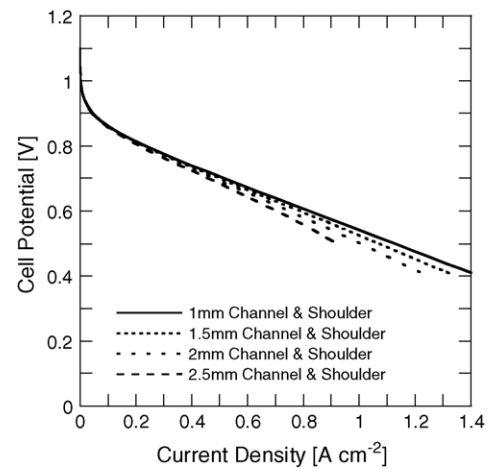
$$\lambda_{avg} = \frac{1}{(L_{sh} + L_{ch}) \cdot t_m} \int_0^{L_{sh}+L_{ch}} \int_0^{t_m} \lambda(x, y)\mathrm{d}x \cdot \mathrm{d}y \quad (40)$$

At low current densities Fig. 4a, the average water content of the membrane was 12.57 mol $H_2O$ (mol $SO_3^-$)$^{-1}$ and as the current density increases the average water content in the membrane reaches 13.83 in Fig. 4b and drops to 13.06 at high current density case Fig. 4c.

### 5.3. Channel size effects

Sensitivity analysis of the channel dimensions, in the range of 1–2.5 mm, on the fuel cell performance is shown in Fig. 5. In all of these cases, the ratio of gas distribution channel to bipolar plate shoulder was kept constant at 1, i.e., equal channel and bipolar shoulder size. The effect of channel dimensions on the fuel cell power density becomes more important at high current density applications. For example, a 1 mm channel and bipolar shoulder has 14% more power than the 2.5 mm channel and shoulder design while operated at 0.6 V; however, power density difference is 11% while the cell is operated at 0.7 V. Performance curves for the 2.5 mm channel and shoulder case clearly shows mass transfer limitations at current density above $0.8\,A\,cm^{-2}$. This is shown by a drop in the performance. The model predicts that a current density of $1\,A\,cm^{-2}$ cannot be obtained with 2.5 mm design due to mass transfer limitations. The 1 mm channel and shoulder case shows a constant slope for moderate to high current density operations up to $1.4\,A\,cm^{-2}$ and it can be concluded that mass transfer limitations to catalyst sites under the bipolar plate shoulder can be prevented by using smaller channels.

#### 5.3.1. Current density profiles

Fig. 6 shows the current density profiles at the cathode catalyst layer for the 1 and 2 mm channel and shoulder cases at three different operating cell potentials 0.9, 0.7, and 0.5 V.
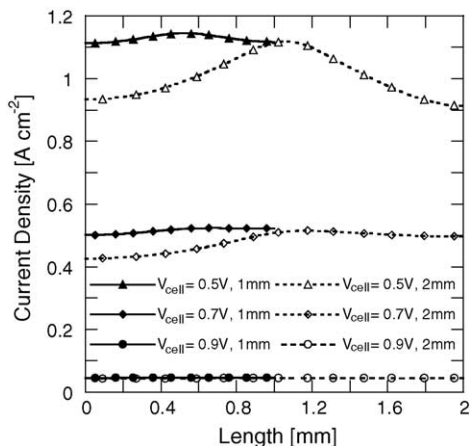
Fig. 6. Current density profiles at the catalyst layer for: 1 mm channel and 1 mm shoulder, 2 mm channel and 2 mm shoulder.



Fig. 7. Hydrogen mole fraction profiles at the anode catalyst layer for: 1 mm channel and 1 mm shoulder, 2 mm channel and 2 mm shoulder.

This figure shows low, moderate, and high current density operations, respectively. The channel and bipolar plate was simplified with symmetry at the center sections of each region so only 0.5 mm of the channel and 0.5 mm of the shoulder is shown in the plot for 1 mm case and 1 mm of channel and shoulder is shown of 2 mm case. Length = 0 is the center of the gas channel and at length = 0.5 mm the bipolar plate shoulder starts touching the electrode for the 1 mm case. At low current density operation, i.e., $V_{cell} = 0.9$ V, the current density profile is uniform for both cases. At moderate current density operation, i.e., $V_{cell} = 0.7$ V the current density increases as it gets closer to the location where the bipolar plate touches the electrode. This increase is due to the low conductivity of the electrode as well as increasing water concentration of the membrane and reduced local membrane resistance. The electrode conductivity of $570 \, \text{S} \, \text{m}^{-1}$ was estimated from the commercial electrode properties and in agreement with the estimate of Nguyen et al. [31]. As we pass the location where the bipolar plate shoulder touches the electrodes, a uniform current density profile is observed suggesting that the concentration change of reactants does not effect the current density profile due to also decreasing membrane resistance. When the current density profiles at the high current density operations was studied, i.e., $V_{cell} = 0.5$ V, the current density profile drop was significant due to a concentration drop of reactants.

### 5.3.2. Concentration profiles

Figs. 7 and 8 show the hydrogen mole fraction at the anode catalyst layer and oxygen mole fraction at the cathode catalyst layers, respectively.

At low current densities the hydrogen mole fraction profile at the anode catalyst layer shows a decrease as it goes under the bipolar plate shoulder. However, at moderate and high current densities the hydrogen mole fraction increases even though hydrogen is consumed at the catalyst. This increase is due to the complex water balance in the PEM fuel cell as shown earlier in Fig. 4. At low current densities, the
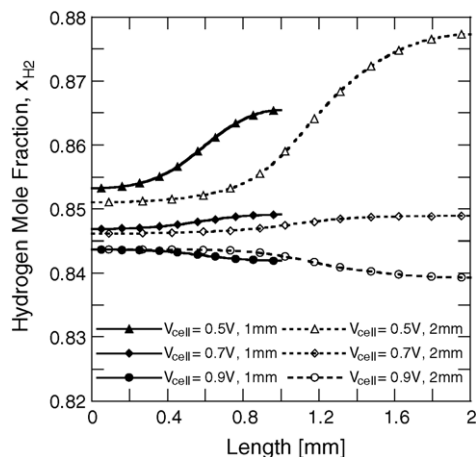
net water flux is from cathode to anode and the hydrogen is consumed at the catalyst layers. This results in a drop of hydrogen mole fraction in Fig. 7; however, at moderate to high current densities the net water flux is from anode to cathode in the membrane. Even at moderate current densities, the magnitude of the net water flux is more than the hydrogen consumption rate thus yielding an increase in mole fraction of hydrogen (Fig. 7 for $V_{cell} = 0.7$ V). The difference of hydrogen mole fractions at length = 0, i.e., the catalyst layer below the center of the gas distribution channel, was due to the difference in current densities as shown in Fig. 6.

The effect of channel and shoulder dimensions on the oxygen mole fraction at the cathode catalyst layer was more significant and is shown in Fig. 8. The complex water transport phenomena in the membrane as well as consumption of oxygen magnifies the mole fraction drop of oxygen at high current density cases. For the 2 mm channel and shoulder case the oxygen mole fraction drops to 0.03. This is the main
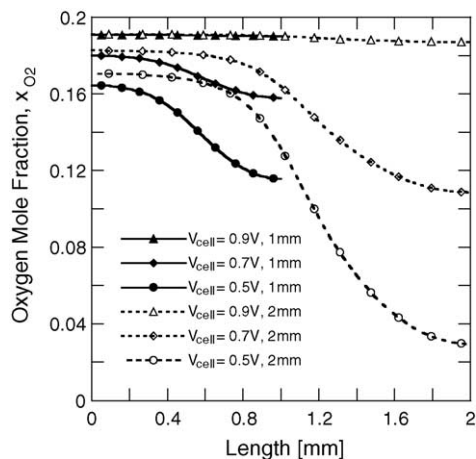


Fig. 8. Oxygen mole fraction profile at the cathode catalyst layer for: 1 mm channel and 1 mm shoulder, 2 mm channel and 2 mm shoulder.
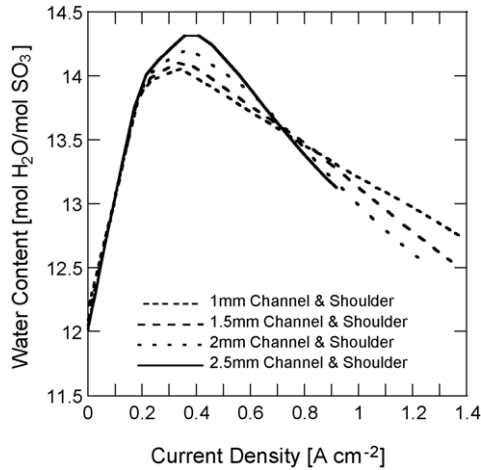
Fig. 9. Average membrane water content for cell.



Fig. 10. Effect of relative humidity of the feed on the performance of the cell.

reason for the drop in current density under the shoulders in Fig. 6 for $V_{cell} = 0.5$. Also, it is worth mentioning that the 2 mm channel and shoulder might not be a proper design for high current density applications. At the exit of the fuel cell, the oxygen mole fraction will be far less than that of this case and may lead to extinction of reactants under the bipolar plates.

### 5.3.3. Water content

Channel and bipolar plate shoulder dimensions do not only effect the mass transfer limitations but also effect the water content of the membrane. Fig. 9 shows the effect of the channel geometry on the average water content of the membrane at different current densities, calculated using Eq. (40).

At current densities below $0.2 \, A \, cm^{-2}$ the average membrane water content is almost the same for all geometries. As the current density increases, the membrane water content also increases. This increase is due to the increasing concentration of water at the cathode catalyst membrane boundary. As the current density increases above $0.2 \, A \, cm^{-2}$ the membrane water content also increases but the rate of increase is smaller compared to current densities below $0.2 \, A \, cm^{-2}$. This is due to an increase in the migrative flux from anode to cathode. The effect of channel and shoulder dimensions on the average membrane content can be seen in Fig. 9. Larger channel and shoulders favor higher membrane hydration at moderate current densities, i.e., $0.2–0.8 \, A \, cm^{-2}$ as the large shoulder area limits the water transport from inside the electrodes under the bipolar plate to channels. The membrane water content reaches its maximum value for all channel and shoulder dimensions between 0.4 and $0.5 \, A \, cm^{-2}$ where the net flux of water becomes zero. As the current density increases above $0.8 \, A \, cm^{-2}$, smaller channel and shoulder dimensions favor higher membrane hydration levels. As the current density increases, the anode side of the membrane dries as can be seen in Fig. 4c, thus increasing the resistance of the membrane.
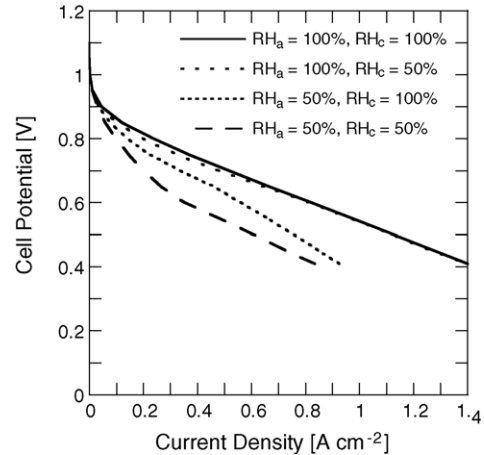
### 5.4. Gas distribution electrode porosity

The effect of porosity of the gas distribution electrodes was also studied and it was found that a reduction of porosity from 0.6 to 0.4 resulted in 2.4% decrease in the average current density for the 1 mm channel and shoulder case operated at 0.6 V. The porosity effect was found to be more significant at higher current density operations and a 6% drop was observed for a fuel cell operating at 0.4 V. The porosity of electrodes is critical for cells with bigger catalyst regions under the bipolar plate shoulders as the supply of the reactants can be rate limiting. For the 2 mm channel and 2 mm shoulder case the reduction of electrode porosity from 0.6 to 0.4 resulted in a 6.6% drop in current density for a fuel cell operated at 0.6 V. Due to insufficient transport of reactants to the catalyst sites, the 2 mm channel and shoulder case could not be operated at higher current densities than $0.85 \, A \, cm^{-2}$.

The water content of the fuel and oxidant streams, of the anode and cathode gases effect the fuel cell performance significantly as shown in Fig. 10. The effect of anode gas inlet relative humidity was found to be one of the most critical operating conditions. A 50% relative humidity of the anode gases was not enough to keep the membrane well hydrated thus resistance of the membrane and ohmic loses at the membrane is higher. The effect of cathode relative humidity was not as critical because at high current densities, water generated at the cathode, and the flow of water is from anode to cathode. At low current densities, less than $0.4 \, A \, cm^{-2}$, the net water flux was from cathode to anode thus the relative humidity effect of the cathode was also low at this region. The 50% relative humidity cathode and saturated anode stream performance curve drops slightly below the saturated anode and cathode stream performance curve between 0.2 and $0.6 \, A \, cm^{-2}$ regions. As the cell was operated at higher current densities the water supplied from the anode side as well as the water generated at the cathode was sufficient to keep the membrane hydrated at high levels.

## 6. Conclusions

A computational fluid dynamics model of a polymer electrolyte membrane fuel cell has been presented. The mass transport, momentum transport, and electrochemical processes occurring in the membrane electrolyte and catalyst layers have been modeled. The effects of channel and bipolar plate shoulder size, porosity of the electrodes, and fuel and oxidant humidification on the cell performance have been studied for a wide range of current densities.

It is found that smaller sized channels and bipolar plate shoulders are required to obtain higher current densities, although larger channels are satisfactory at moderate current densities. If the application requires bigger channel and shoulder sizes, increasing the porosity of the gas distribution electrode helps the mass transport.

The effect of the relative humidity of the anode gas stream was found to be the most critical condition affecting the performance of the fuel cell. Also, the fuel cell design, the geometric dimensions of the channels and bipolar plate shoulders, the thickness of electrodes, and membrane, and the porosity of the electrodes and conductivity of the electrodes needs to be selected carefully for different applications.

The development of this FEMLAB$^{®}$ model enables us to study operating conditions and design parameters from a CFD model and optimization algorithms available in MATLAB$^{®}$. The selected 2D domain enabled us to study the effects of channel and shoulder sizes, which along the channel 2D models lack. However, the concentration changes along the channel and their effect on the performance of the entire fuel cell cannot be captured with this model. Future work will focus on developing a procedure to evaluate the entire fuel cell performance with multiple evaluations of the 2D model along the channel. The operating conditions and selection of components for different applications can then be optimized. The robustness and typical convergence speed of under 150 s with a desktop PC is a crucial benefit of this model and will enable CFD optimization to be a practical application.

## References

[1] D.M. Bernardi, M.W. Vebrunge, A mathematical model of the solid-polymer-electrolyte fuel cell, J. Electrochem. Soc. 139 (9) (1992) 2477–2491.

[2] T.E. Springer, T.A. Zawodzinski, S. Gottesfeld, Polymer electrolyte fuel cell model, J. Electrochem. Soc. 138 (8) (1991) 2334–2342.

[3] T.F. Fuller, J. Newman, Water and thermal management in solid polymer electrolyte fuel cell, J. Electrochem. Soc. 140 (5) (1993) 1218–1225.

[4] T.V. Nguyen, R.E. White, A water and thermal management model for proton exchange membrane fuel cells, J. Electrochem. Soc. 140 (8) (1993) 2178–2186.

[5] J.J. Baschuk, X. Li, Modeling of polymer electrolyte membrane fuel cells with variable degrees of water flooding, J. Power Sources 86 (2000) 181–196.

[6] J.J. Baschuk, X. Li, Carbon monoxide poisoning of proton exchange membrane fuel cells, Int. Energy Res. 25 (8) (2001) 695–713.

[7] V. Gurau, H. Liu, S. Kakac, Two-dimensional model for proton exchange membrane fuel cells, AIChE J. 44 (11) (1998) 2410–2422.

[8] S. Um, C.-Y. Wang, K.S. Chen, Computational fluid dynamics modeling of proton exchange membrane fuel cells, J. Electrochem. Soc. 147 (12) (2000) 4485–4493.

[9] S. Um, C.Y. Wang, Three-dimensional analysis of transport and electrochemical reactions in polymer electrolyte fuel cells, J. Power Sources 125 (2004) 40–51.

[10] H. Meng, C.Y. Wang, Large-scale simulation of polymer electrolyte fuel cells by parallel computing, Chem. Eng. Sci. 59 (2004) 3331–3343.

[11] U. Pasaogullari, C.Y. Wang, Two-phase transport and the role of micro-porous layer in polymer electrolyte fuel cells, Electrochim. Acta 49 (2004) 4359–4369.

[12] T. Berning, D.M. Lu, N. Djilali, Three-dimensional computational analysis of transport phenomena in a PEM fuel cell, J. Power Sources 106 (2002) 284–294.

[13] T. Berning, N. Djilali, Three-dimensional computational analysis of transport phenomena in a PEM fuel cell—a parametric study, J. Power Sources 124 (2003) 440–452.

[14] T. Berning, N. Djilali, A 3D, multiphase, multicomponent model of the cathode and anode of a PEM fuel cell, J. Electrochem. Soc. 150 (12) (2003) A1598–A1607.

[15] M. Grujicic, K.M. Chittajallu, Design and optimization of polymer electrolyte membrane (PEM) fuel cells, Appl. Surf. Sci. 227 (2004) 56–72.

[16] Fluent 6.1, User's Guide, Fluent Inc., 2003.

[17] CFX-5, ANSYS Inc., Canonsburg, PA, 2004.

[18] STAR-CD V3.22, CD-adapco Group, Melville, NY, 2004.

[19] FEMLAB 3.0 User Guide, COMSOL Inc., Burlington, MA, 2004.

[20] V. Mehta, J.S. Cooper, Review and analysis of PEM fuel cell design and manufacturing, J. Power Sources 114 (2003) 32–53.

[21] R.B. Bird, W.E. Stewart, E.N. Lightfoot, Transport Phenomena, second ed., John Wiley & Sons, Inc., 2002.

[22] S. Motupally, A.J. Becker, J.W. Weidner, Diffusion of water in Nafion 115 membranes, J. Electrochem. Soc. 147 (9) (2000) 3171.

[23] T.A. Zawodzinski, J. Davey, J. Valerio, S. Gottesfeld, The water content dependence of electro-osmotic drag in proton-conducting polymer electrolytes, Electrochim. Acta 40 (3) (1995) 297–302.

[24] T.A. Zawodzinki, T.E. Springer, F. Uribe, S. Gottesfeld, Characterization of polymer electrolytes for fuel cell applications, Solid State Ionics 60 (1993) 199–211.

[25] R.H. Perry, D.W. Green, Perry's Chemical Engineer's Handbook, seventh ed., 1997.

[26] A.J. Bard, L.R. Faulkner, Electrochemical Methods, Wiley, New York, 1980.

[27] A. Parthasarathy, S. Srinivasan, A.J. Appleby, Temperature dependence of the electrode kinetics of oxygen reduction at the platinum/nafion interface—a microelectrode investigation, J. Electrochem. Soc. 139 (1992) 2530–2537.

[28] MATLAB 7.0, The MathWorks Inc., Natick, MA, 2004.

[29] E.A. Ticianelli, C.R. Derouin, S. Srinivasan, Localization of platinum in low catalyst loading electrodes to attain high power densities in SPE fuel cells, J. Electroanal. Chem. 251 (1988) 275–295.

[30] M.M. Mench, Q.L. Dong, C.Y. Wang, In situ water distribution measurements in a polymer electrolyte fuel cell, J. Power Sources 124 (2003) 90–98.

[31] P.T. Nguyen, T. Berning, N. Djilali, Computational model of a PEM fuel cell with serpentine gas flow channels, J. Power Sources 130 (2004) 14–157.

[32] R.C. Reid, J.M. Prausnitz, B.E. Poling, The Properties of Gases and Liquids, fourth ed., McGraw-Hill, New York, 1987.